RESEARCH ARTICLE

High-Isolation Wide-Band Four-Element MIMO Antenna Covering Ka-Band for 5G Wireless Applications

PARVEEZ SHARIFF B. G.[1], (Student Member, IEEE), **AKSHAY ANIL NAIK**[1],
TANWEER ALI[1], (Senior Member, IEEE), **PALLAVI R. MANE**[1], (Senior Member, IEEE),
RAJIV MOHAN DAVID[1], **SAMEENA PATHAN**[2], **AND JAUME ANGUERA**[3,4], (Fellow, IEEE)

[1]Department of Electronics and Communication Engineering, Manipal Institute of Technology, Manipal Academy of Higher Education, Manipal 576104, India
[2]Department of Information and Communication Technology, Manipal Institute of Technology, Manipal Academy of Higher Education, Manipal 576104, India
[3]Ignion, 08174 Barcelona, Spain
[4]Research Group on Smart Society, La Salle Engineering, Universitat Ramon Llull, 08022 Barcelona, Spain

Corresponding authors: Tanweer Ali (tanweer.ali@manipal.edu) and Rajiv Mohan David (rajiv.md@manipal.edu)

ABSTRACT The wireless communication system is steered towards the millimeter wave spectrum to achieve low latency and high-speed data rate. The MIMO antennas aid in attaining a higher data rate. The prominent spectrum at millimeter wave is Ka-band, suitable for short-range communication. The |S-parameter| response and radiation pattern of the existing MIMO antenna at this band are relatively unstable. Hence it encouraged to design and develop a four-element MIMO antenna operating at Ka-band. The antenna is a circular ring shape with two concentric rings with a plus-shape stub overlayed on circular rings. The structure is developed in four-stage with the comprehension of characteristic mode theory (CMA). The proposed structure generated Mode 2 as an efficient mode, with minor Modes 3 and 5 contributing for resonance out of five modes. The overall antenna profile is $3.27\lambda_0 \times 3.74\lambda_0$ (where λ_0 is the wavelength at a resonance frequency of 28 GHz). The novel decoupling structure has improved the isolation to 30 dB and increased the bandwidth. The antenna has an operating bandwidth of 24.1-30.9 GHz, with a maximum gain of 6.5 dBi. The |S-parameter| from all the ports has an exact and stable response. The proposed antenna has resulted in bidirectional radiation tilted at an angle of 334^0 and 210^0 in the XZ plane. In the YZ plane, it has a triple beam. The radiation pattern is also stable throughout the bandwidth. The proposed MIMO antenna has a symmetrical design, demonstrating the possibility of expansion to n-element MIMO through a six-element MIMO antenna design. The article also presents the channel capacity, path loss, and link margin calculation for designed antenna line-of-sight (LOS) communication. The antenna has been evaluated with diversity parameters such as ECC, DC, CCL, TARC, and MEG.

I. INTRODUCTION

The demand for higher data rates in wireless communication systems has compelled us to switch to the millimeter wave (mmWave) spectrum. However, the hindrance at mmWave is signal attenuation due to atmospheric conditions.

The associate editor coordinating the review of this manuscript and approving it for publication was Sawyer Duane Campbell.

The Ka-band (26-40 GHz) is less prone to atmospheric conditions [1]. Therefore, it makes it suitable for short-range communication. There are many antennas have been designed to operate at millimeter wave bands. In these, planar antennas are cost-efficient and compact compared to other antennas; many such antennas are presented in [2]. The Multiple-Input-Multiple-Output (MIMO) antenna system further boosts the channel capacity [3]. The challenge

in the planar compact MIMO antenna is port isolation. It deteriorates the bandwidth and radiation performance of an antenna. There are methods like decoupling structure [4], [5] self-decoupling structure [6], and metamaterial cells [7], [8] which aid in regulating the surface wave and enhance the port isolation.

In [9], a U-shape monopole antenna with two elements is proposed. The antenna has a wide bandwidth of 27-32.5 GHz. The antenna profile is $2.81\lambda_0 \times 1.4\lambda_0$. However, the isolation is low at lower frequencies, that is, 17.5 dB. Also, it is unstable over the band of interest. In [10], a two-element, orthogonally oriented T-shape monopole antenna with an offset feed and appended stub at 45^0 generated radiation in the end-fire direction. It operates with a bandwidth of 26-30 GHz. However, the |Sii| response of both ports is not shown. Another two-element MIMO antenna of an S-shape radiator structure is presented in [11]. The antenna has a good isolation of 30 dB. However, the bandwidth is narrow to 27.5-29.8 GHz. Also, both port's reflection coefficient |Sii| curves are unstable. In [12], an inverted E-shape two-element MIMO antenna is proposed. Here, the |S-parameter| of a two-element antenna for different orientations is studied. Out of which, the inverted orientation has resulted in a better bandwidth of 25.5-30 GHz. A dipole shape, two-element MIMO antenna with a T-shape decoupling structure in the ground plane is proposed in [13]. This article has presented only simulated |S-parameter|, which has a 24.6-42.1 GHz bandwidth. In [6], a two-element self-isolating MIMO antenna is proposed. The radiator is a conventional patch with an offset feed. To enhance the isolation, the element is bent by 45^0, and two slits are etched on the horizontal edges of the patch. However, it has a lower bandwidth from 28.8-29.75 GHz, and isolation is 22 dB.

Further in [14], an orthogonal-orientated four-element MIMO antenna is presented. The single element is a circular patch with slits on either side. The slits are introduced to enhance the bandwidth at 28 GHz. The MIMO antenna operates from 26.5-29.5 GHz. A corrugated ground plane structure is proposed in this article, which improved the isolation. The antenna profile is $2.85\lambda_0 \times 2.85\lambda_0$. Another orthogonal-orientated four-element MIMO antenna is proposed in [15]. The radiator is a monopole with imbricated circular rings. The antenna size is $2.85\lambda_0 \times 2.85\lambda_0$. The antenna operates from 27.2-29.2 GHz, with an isolation of 29 dB. However, the design has certain limitations. Its ground plane is disconnected, and all four elements |Sii| results vary. Another orthogonally oriented four-element MIMO antenna is presented in [16]. The antenna is a monopole with a four-arc shape design. The multiple arcs are to generate multiple resonances. The antenna operates from 24-38 GHz, having port-to-port isolation of 22 dB. However, it has a large antenna profile of $7.47\lambda_0 \times 7.47\lambda_0$. Also, the variation in reflection coefficient |Sii| from MIMO elements can be observed.

A tapper slot four-element MIMO antenna is proposed in [17]. It is fed by an L-shaped feed. The antenna resonance depends on the tapered angle and feed length. The antenna dimension is $9.47\lambda_0 \times 9.47\lambda_0$. However, the reflection coefficient |S11| from 22-26 GHz is close to 10 dB, with an overall bandwidth of 22-30 GHz. Also, the |Sii| response of all four elements varies. The isolation |Sij| (where i $\neq$ j) is 22 dB. Another design proposes an inverted C-shape four-port MIMO antenna [18]. Each port has a two-element array. The antenna has a bandwidth from 26-30 GHz, with an isolation of 22 dB. The antenna profile is $10.3\lambda_0 \times 7\lambda_0$. Though the gain is high, the |Sii| is not stable.

A four-port MIMO antenna, each with a two-element array with orthogonal orientation, is proposed in [19]. It has a narrow bandwidth of 27.5-28.5 GHz. With the decoupling structure, the isolation is enhanced to 35 dB. However, the antenna profile is large, which is $2.81\lambda_0 \times 3.27\lambda_0$. In [20], a four-element MIMO circular patch antenna is proposed. The elements are orthogonally arranged. The radiator is etched with an elliptical slot to tune the resonance at 28 GHz. It has a bandwidth of 26.5-31 GHz. However, the ground structure of the four elements is disconnected. Also, the isolation is low at 17.5 dB. In [21], a four-element orthogonal oriented MIMO antenna of petal shape radiator is presented. The ground plane is defected to enhance the bandwidth, which operates from 27-29 GHz. The antenna profile is $2.33\lambda_0 \times 1.4\lambda_0$. However, the grounds of MIMO elements are disconnected. Also, the isolation is low at 17 dB. Another orthogonal-oriented four-element MIMO is proposed in [22]. The radiator is a flipped S-shape monopole antenna. To enhance the isolation, a four-blade fan shape decoupling structure is carved between the radiator. It has a bandwidth from 22-40 GHz, with an isolation of 21 dB. However, the ground plane of elements is disconnected. In [23], a four-port, eight-element MIMO antenna is proposed. The radiator is a modified C-shaped structure with a stub at the center. The ground plane is defected with slots to improve the isolation. It operates from 26.2-29.5 GHz. The antenna dimension is $2.91\lambda_0 \times 3.39\lambda_0$. However, the isolation is low at 10 dB; also the |S-parameter| is also unstable.

The following observations are made from the above state-of-the-art designs: Most of the designs are orthogonally oriented to obtain better isolation. However, such designs are non-expandable. Most designs have disconnected grounds [15], [20], [21], [22], which is not an acceptable practice [24]. Some designs have narrow bandwidth [6], [11]. Few designs have low port isolation [9], [21], hindering antenna performance. Some designs have large antenna profiles [16], [17], [18]. A few design reflection coefficients |Sii| characteristic graphs of MIMO elements are unstable [10], [15], [18], [23]. Therefore, this article addresses the above issues and presents a compact, stable, wideband four-element MIMO antenna operating at Ka-band with good isolation.

The proposed antenna profile is $3.27\lambda_0 \times 3.74\lambda_0$ (where λ_0 is the wavelength at resonance frequency f_0 of 28 GHz), which is smaller than [16], [17], and [18] and relatively comparable with the [14], [15], [19], and [23]. Most MIMO antennas in the literature have an orthogonal structure,

which limits itself from a scalability perspective. However, the proposed MIMO antenna structure has a symmetrical arrangement, which gives the flexibility to expand the antenna to n-element MIMO based on the application requirements. To support this, the geometry of an antenna and proposed decoupling structure becomes vital in regulating the surface waves, thereby generating stable |S-parameter| and radiation patterns.

The following are the contributions of the article:

1. The characteristics mode theory is applied to analyze the antenna element and to excite Mode 2.
2. Generation of stable reflection coefficient |Sii| response from four-elements of MIMO antenna with enhanced bandwidth at $f_0 = 28.5$ GHz.
3. A unique decoupling structure (DCS) is proposed to enhance the isolation and bandwidth.

The flow of the article is as follows: Section II presents the single-element antenna development stages through CMA, followed by the four-element MIMO antenna configuration in Section III. Section IV presents the results and discussions, followed by the scalability of the proposed antenna in 5. Section VI discusses antenna validation in the communication scenario, followed by a comparative analysis in Section VII, and the conclusion is in Section VIII.

II. ANTENNA CONFIGURATION
The design of the Ka-band single-element antenna progressively emerged from four stages. The first stage has a circular ring fed by a 50 Ω feed line. The circular ring is obtained by etching two circular patches using equations defined in [25]. The structure is carved on Rogers 5880 substrate, which has a thickness of 0.254 mm. The bottom of the substrate has a full ground plane, as depicted in Fig. 1(a). In stage 2, another circular ring stub is engraved inside the radiator ring, which is connected by a rectangular stub in Fig. 1(b). In stage 3, a plus-shape stub is carved on the radiator ring in Fig. 1(c). Finally, in stage 4, the ground plane is defected, representing a T-shape structure in Fig. 1(d).
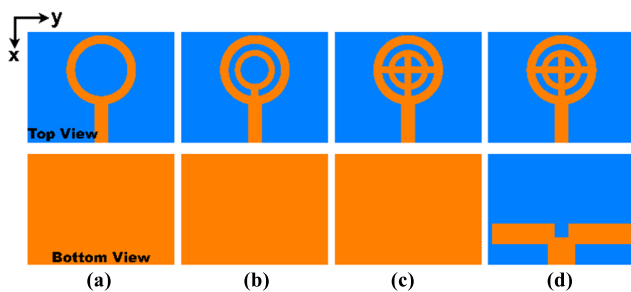
FIGURE 1. Development stages of antenna. (a) Stage 1, (b) stage 2, (c) stage 3, and (d) stage 4.

CMA is a tool that aids in rapidly developing an antenna design. Previously, many arbitrary-shaped antenna structures were designed using CMA [26], [27]. The CMA predicts the surface current from the antenna structure

through which it estimates the performance and radiation pattern [28], [29], [30]. Therefore, the above stages in this article progressively evolved through the characteristics mode theory (CMA) analysis. The CMA analyzes the structure surface current (J), and represent in terms of the eigenvalue (λ_n) and eigen-current (J_n), as in [27] and [31]. The solution to the eigenvalue leads to the modal significance (MS) and characteristic angle (CA). The MS = 1 defines the significant modes contributing to the generation of resonance in the structure. However, few modes of the structures often do not completely radiate the energy coupled. These modes store energy in electric or magnetic fields, compromising antenna performance. Such modes can be clearly studied by eigenvalue (λ_n) and CA. When the $\lambda_n = 0$ and the phase of the mode CA = 180^0, it is an efficient mode [32]. It means it radiates most of the energy coupled to it. When $\lambda_n < 0$ and $180^0 \leq CA \leq 270^0$, the mode stores electric field, which acts as a capacitive mode. When $\lambda_n > 0$ and $90^0 \leq CA \leq 180^0$, the mode stores the magnetic field, and behaves as an inductive mode [32]. The inductive or capacitive modes must be suppressed or improved by perturbing the structures current flow. It is achieved by modifying the physical structure of the antenna. The surface current of respective modes generates unique radiation patterns. Therefore, the CMA aids antenna development and obtains the desired radiation pattern.
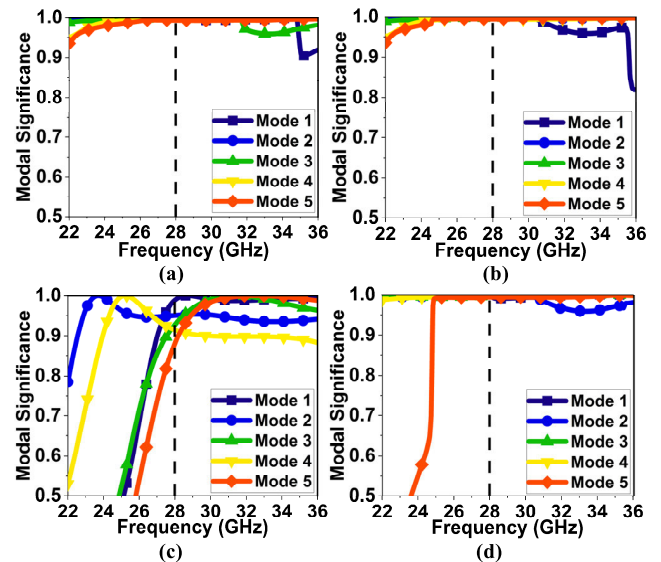
FIGURE 2. Modal Significance (MS) graph at f_0 for (a) stage 1, (b) stage 2, (c) stage 3, and (d) stage 4 antenna.

To begin with, the number of modes chosen is five because most of the significant modes lie within these, and rarely any mode seen beyond it [33]. Therefore, the antenna of stage 1 in Fig. 1(a) is sorted at frequency f_0 (28 GHz) for five modes. MS in Fig. 2(a) indicates that all five Modes are significant with a value close to 1. However, the (λ_n) and CA in Figs. 3(a) & 4(a) clarify that Modes 1 and 2 are efficient resonant modes at 26.2 GHz with a bandwidth of 26-27 GHz. Beyond these

frequencies, these modes become capacitive and inductive. Modes 3 to 5 are slightly capacitive over 25-29.5 GHz. It is to be noted that the capacitive modes also contribute to the resonance [27].
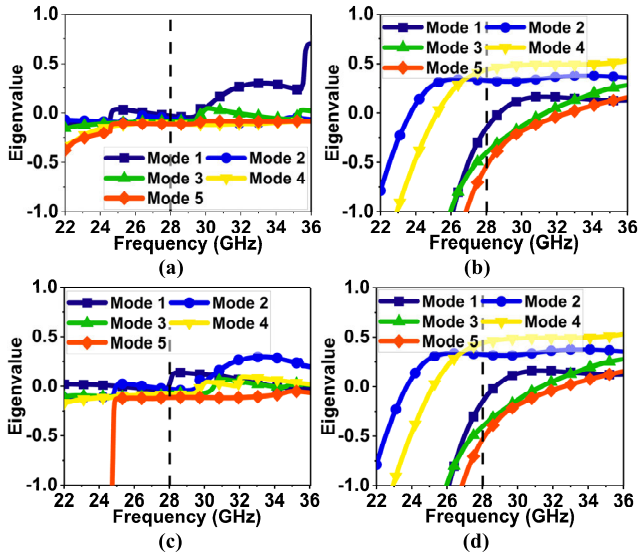

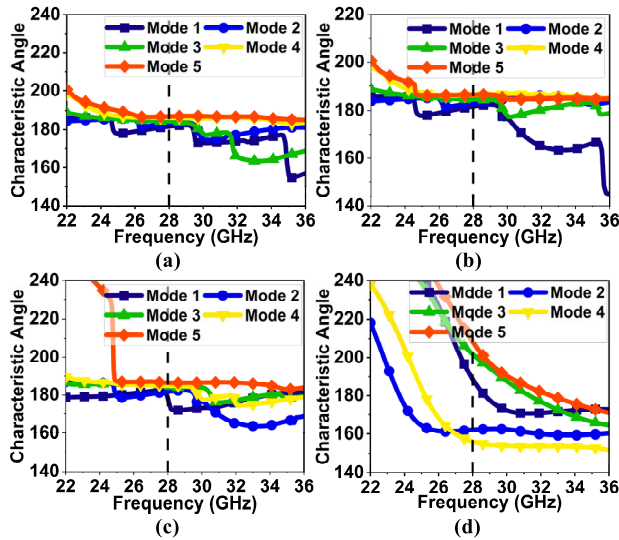FIGURE 3. Eigenvalue (λ_n) graph at f_0 for (a) stage 1, (b) stage 2, (c) stage 3, and (d) stage 4 antenna.

FIGURE 4. Characteristic Angle (CA) graph at f_0 for (a) stage 1, (b) stage 2, (c) stage 3, and (d) stage 4 antenna.

The modal surface current (J_n) can envisage the radiation pattern of modes at respective stages. In this stage, the modal surface current (J_n) in Fig.5 at Mode 1 has an in-phase current with equal magnitude along the vertical edges of the ground plane (black arrow). The horizontal edges have an anti-phase current. Therefore, it resulted in bidirectional radiation at $\varphi = 0$ and has a quad-beam at $\varphi = 90^0$ [34]. Likewise, Mode 2 has in-phase and anti-phase currents along vertical and horizontal edges of the ground, resulting in quad-beam and bidirectional radiation at $\varphi = 0$ and $\varphi = 90^0$.

However, Modes 4 and 5 have in-phase current in the radiator (red arrow), resulting in bidirectional radiation at $\varphi = 0$ and $\varphi = 90^0$. Therefore, it can be concluded that the combination of in-phase and anti-phase currents generates bidirectional radiation with quad-beam, whereas only in-phase current generates bidirectional radiation.
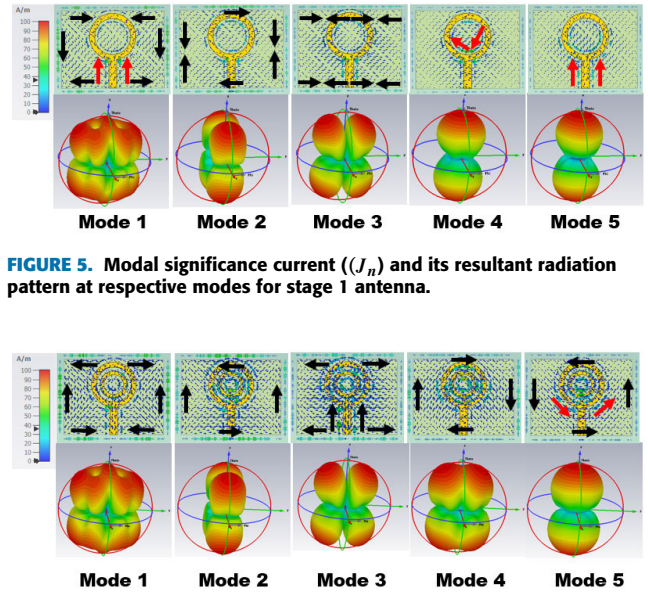

FIGURE 5. Modal significance current ((J_n)) and its resultant radiation pattern at respective modes for stage 1 antenna.

FIGURE 6. Modal significance current ((J_n)) and its resultant radiation pattern at respective modes for stage 2 antenna.

An addition of a circular ring inside the outer ring in stage 2 perturbed the surface current J_n at all modes, as indicated in Fig. 6. In this case, all modes appear to be significant in Fig. 2(b) at f_0. Also, the convergence of the eigenvalue to zero in Fig. 3(b) indicates the same. However, the CA in Fig. 4(b) reveals Modes 1 to 3 have a bandwidth from 26-29 GHz, whereas Modes 4 and 5 have a wide bandwidth from 24-36 GHz, but these have minor capacitive effects. The antenna in stage 3 (Fig. 1(c)) incorporates the plus-shape stub on the radiator circle, which increases the current oscillation (red arrow), as shown in Fig. 7. At this stage, as well, all modes continue to be significant, as depicted in Fig. 2(c). The eigenvalue of these modes in Fig. 3(c) converges to zero at f_0 but with a narrow bandwidth. The CA indicates Mode 1 and 2 transform from efficient resonant mode to inductive mode beyond f_0, in Fig. 4(c).

Though in the previous design, all five modes look prominent, their cumulative effect restricts the antenna performance in terms of bandwidth. Hence, the ground plane is modified in stage 4 (Fig. 1(d)). The modification to the structure has sorted the modes at different resonances, suppressing others. As can be seen in Fig. 2(d), Mode 1 is significant at 23.4 GHz, Mode 2 at 28 GHz, Modes 3 and 5 at 31 GHz, and Mode 4 at 25 GHz. To comprehend the efficient resonant mode, eigenvalue λ_n, and CA graphs of Figs. 3(d) and 4(d) to be considered. The eigenvalue reveals Mode 2 is convergent to zero at f_0, becoming the dominant resonant mode. The CA

indicates that Modes 3 and 5 are capacitive and converge close to the 180^0 phase angle. The surface current (Fig. 8) at Mode 1 has an in-phase current in the ground plane (black arrow) and an anti-phase current in the radiator (red arrow), resulting in bidirectional radiation at $\varphi = 0$ and hexa-beam at $\varphi = 90^0$. In the case of Modes 2, 3, and 5, the current in the radiator has an in-phase current. However, in the ground plane, the current is in the horizontal edges with in-phase, but in the opposite direction. Therefore, both result in bidirectional radiation but nulls at different φ. Therefore, the proposed single-element antenna has a single dominant resonant mode (Mode 2) and two minorly contributing modes (Modes 3 and 5) operating over 27-30 GHz.
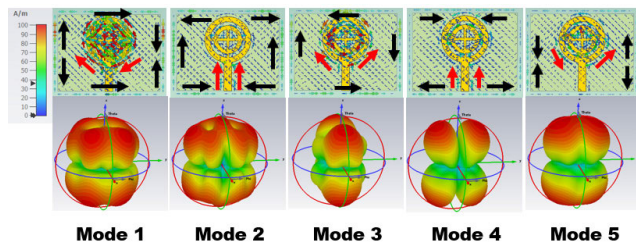

FIGURE 7. Modal significance current ((J_n) and its resultant radiation pattern at respective modes for stage 3 antenna.
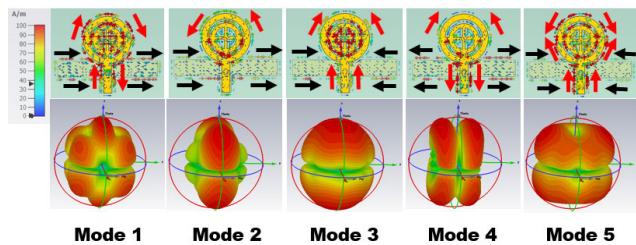

FIGURE 8. Modal significance current ((J_n) and its resultant radiation pattern at respective modes for stage 4 antenna.

Figs. 9(a & b) shows the final dimensions of the proposed single-element antenna. The dimension variables are indicated in mm, which are as follows: $ST_W = 0.5$, $R_1 = 4.5$, $R_2 = 3.5$, $R_3 = 2.75$, $R_4 = 2$, $SB_W = 20$, $SB_L = 15$, $F_L = 5.55$, $F_W = 1.5$, $GW_1 = 2$, $GL_1 = 3$, $GW_2 = 19$, $GL_2 = 3$, $GW_3 = 1$, and $GL_3 = 1.5$. The above CMA analysis is performed through surface excitation. However, when the antenna port is excited, the reflection coefficient |S11| for different stages is displayed in Fig. 9(c). Therefore, the stage 4 proposed antenna resonates at $f_0 = 28$ GHz, with a wide bandwidth from 24.3-31.7 GHz.
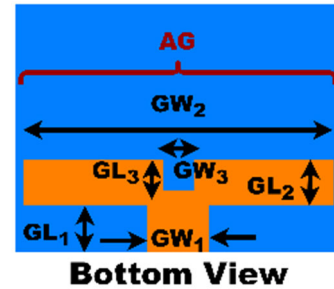
The resonance f_0 can also be calculated using equation (1).

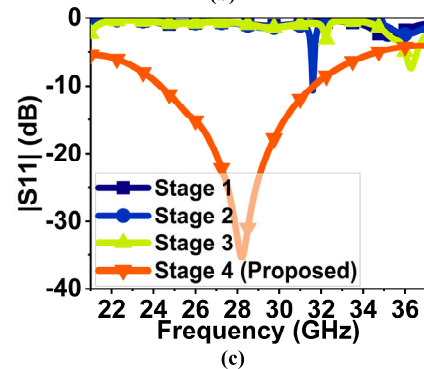$$f_0 = \frac{c}{k \times \frac{2}{\pi} \times TA \times \sqrt{\varepsilon_r}} \quad (1)$$

where $k = 0.1$ (tunable variable), TA is the total conducting area above and below the substrate, and $\varepsilon_r = 2.2$ is substrate permittivity. The total area (TA) can be calculated as the sum of the area of the radiator (AR) and the area of the ground (AG), as indicated in Figs. 9(a & b).
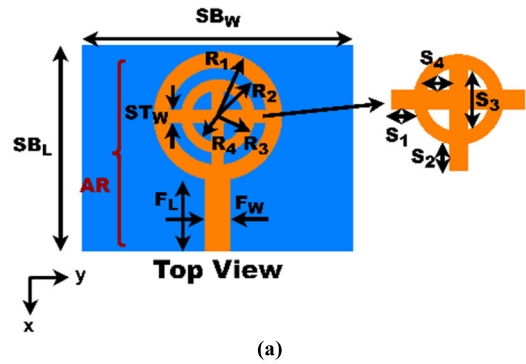
FIGURE 9. Proposed single-element antenna. (a) Top view, (b) bottom view, and (c) reflection coefficient |S11| curves after excitation from respective stages.

A. EQUIVALENT CIRCUIT OF SINGLE-ELEMENT ANTENNA

The reflection coefficient |S11| of the above-designed antenna is realized by an equivalent circuit model, as shown in Fig. 10. The realized circuit has two parallel RLC networks having an impedance of Z1 and Z2, three series RLC networks with an impedance of Z3, Z4, and Z5, and a load resistor with impedance ZL = 50 Ω. The SRx, SLx, and SCx represent the network resistance, inductance, and capacitance, where x ranges from 1 to 5. The RLC values of the equivalent circuit are listed in Table 1. Fig. 11 shows the |S11| response of the simulated antenna and equivalent RLC circuit. The two parallel RLC circuit behaves as bandpass filters from f_1 to f_2, with an impedance Z1 $\approx$ Z2 $\approx$ 50 Ω. These two circuits generate the resonance at f_0. The three series RLC circuits have higher impedance > 300 Ω, which generates the notch below f_1 and above f_2, behaving as a bandstop filter. Therefore, the entire RLC circuit acts as a quarter-wave

transform to deliver the entire input power from port 1 to the load resistance RL.
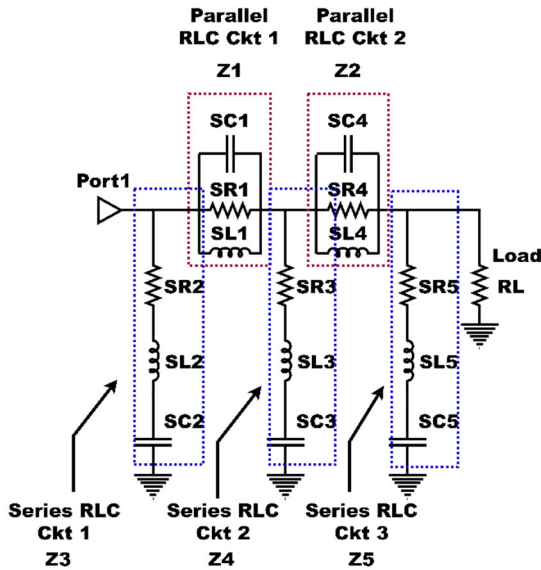

FIGURE 10. RLC equivalent circuit model of single-element antenna.

TABLE 1. RLC values of a single-element equivalent circuit.

Parameter	Value	Parameter	Value
SR1	352	SR2	582
SR3	528	SR4	468
SR5	302.5	SRL	50
SC1	0.142	SC2	0.023
SC3	0.046	SC4	0.155
SC5	0.219	SL1	0.93
SL2	1.235	SL3	3.89
SL4	0.125	SL5	0.325

Note: Resistance R is in ohms, Inductance L is in nH, and capacitance C is in pF.
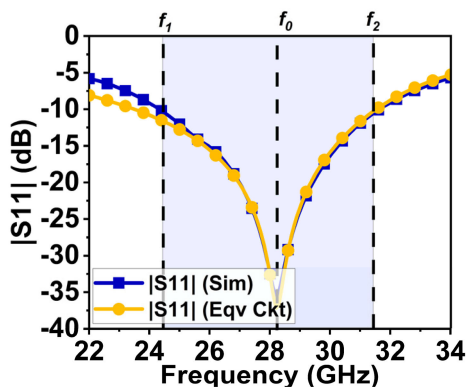

FIGURE 11. |S11| response of simulated antenna and its equivalent RLC circuit.

III. FOUR-ELEMENT MIMO ANTENNA

The single-element antenna is extended to a four-element MIMO antenna to enhance the channel capacity through spatial multiplexing in a lossy environment. Equation (2) indicates the direct relation of channel capacity (C) with signal-to-noise ratio *(SNR)* and MIMO antenna setup (*where HH* - Hermitian matrix*) [35], [36]. The equation assumes the channel fading information is unknown.

$$C = log_2 \left(det \left(I_N + \frac{SNR}{n} HH^* \right) \right) \tag{2}$$

A four-element MIMO antenna arrangement has two horizontally adjacent elements with the radiator-to-radiator distance $RR_H = 1.03\lambda_0$. The other two elements are vertically mirrored with a distance $RR_V = 0.56\lambda_0$, as shown in Fig. 12(a) (top view). The ground plane of all four ports is connected through a rectangular stub ID, as displayed in Fig. 12(a) (bottom view). The ID also behaves as a neutralization line between ports 1 & 2 to 3 & 4. Line N1 and N2 curb the surface wave coupling between adjacent elements between ports 1 and 2 and ports 3 and 4. Therefore, the line ID, N1, and N2 form the ground plane decoupling structure (DCS).

To analyze the surface wave coupling and observe the MIMOs isolation level, let us consider the surface wave current image when port 1 is excited, as shown in Fig. 13(a). Due to port excitation and connected ground, the surface wave current from radiator one (Port 1) is coupled to radiators 2, 3, and 4. The excitation also generates a reverse current on lines N1, ID, and N2, which neutralizes the coupling current from radiator one (Port 1). However, the port isolation between adjacent elements |S21|/|S12| and |S43|/|S34| is low at 19.5 dB. It indicates that lines N1 and N2 are inefficient in curbing the surface wave coupling. On the other hand, the line ID is analogously better with isolation |S31| of 22.7 dB and |S41| of 21.76 dB. The decoupling structure also has an impact on the bandwidth. It has reduced the bandwidth to 25.5-31.58 GHz, with resonance at $f_0 = 28$ GHz, as displayed in Fig. 14(a). Also, the isolation is not stable over the bandwidth.

The decoupling structure is revised in Fig. 12(b) to obtain a stable response in the band of interest. The line ID in the ground plane is replaced with lines N3, N4, N5, N6, and rectangular ring NR, as depicted in Fig. 12(b) (bottom view). From the surface wave current distribution in Fig. 13(b), it can be observed that line N3 artifices the surface wave current from port 1 when it is excited. On the other hand, NR and N4 neutralize the current on N1, resulting in stable and good isolation |S21| > 23.5 dB. Also, the DCS has resulted in better isolation |S31| and |S41| of > 24 dB and >25.4 dB, as displayed in Fig. 13(b). The DCS has also improved the bandwidth to 24.1-31.72 GHz. However, the resonance is shifted higher to $f_0 = 28.5$ GHz. The dimensions of the four-element MIMO antenna in mm are presented in Table 2.
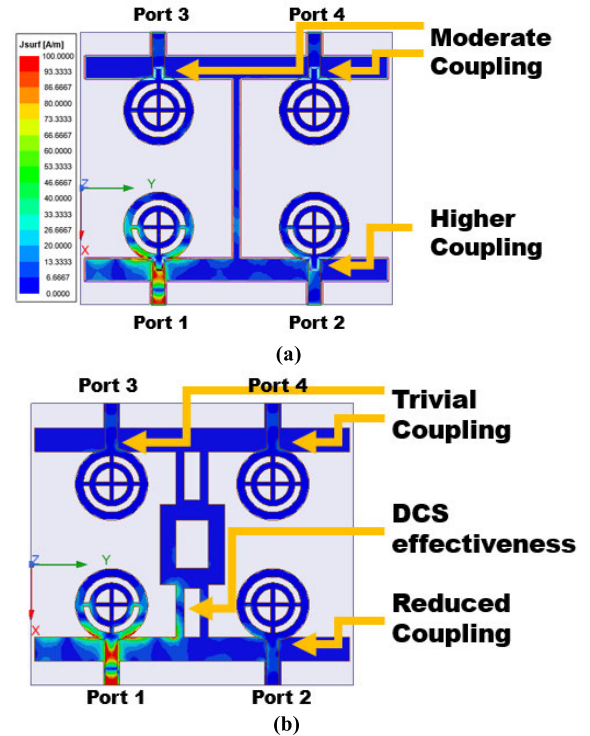
A. EQUIVALENT CIRCUIT OF PROPOSED DCS

The proposed DCS in Fig. 12(b) is modeled through inductance and capacitance LC equivalent circuits, as shown in Fig. 15(a). The conductive lines in DCS are represented by inductance and the gap between them by capacitance. Inductance L1, L4, and L5 exhibit the line N1.
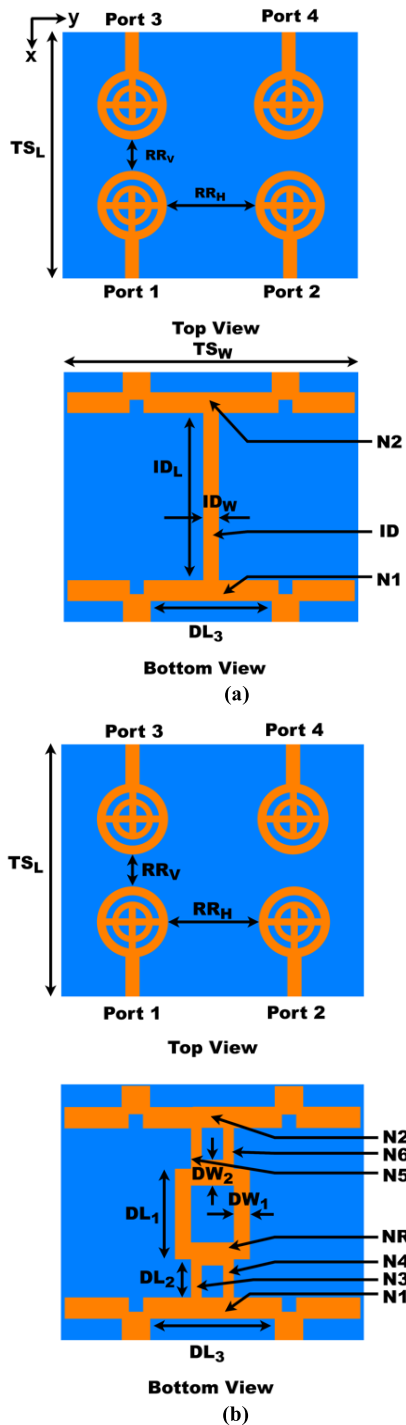
FIGURE 12. (a) Proposed four-element MIMO antenna with initial decoupling structure. (b) Proposed four-element MIMO antenna with final decoupling structure.

FIGURE 13. Influence of surface wave current on adjacent and opposite elements. (a) For initial DCS structure. (b) For proposed DCS structure.

TABLE 2. Ground plane dimensions of four-element MIMO antenna (in mm).

Parameter	Dimension	Parameter	Dimension
TS_L	35	TS_W	40
RR_H	11	RR_V	6
ID_W	1	ID_L	23
DL_1	10	DL_2	6.5
DL_3	18	DW_1	2
DW_2	2.5		

C4 represents the gap in the middle. L18 and L17, and the gap by C7 represents the lines N5 and N6. L16, L15, and L12 imitate the line N2, the notches by capacitance C6 and C5. L13 and L14 represent the open circuit on N2. For the analysis purpose, L1, L2, L3, L4, L5, C1, and C2 are tuned to match the |S21| simulation curve, as depicted in Fig. 15(b). Likewise, to obtain the |S31| curve, L1, L3, L4, L6, L7, L8, L9, L18, L16, L13, L12, C1, C3, C4, C7 and C6 need to be tuned. The final tuned values of LC are mentioned in Table 3.

IV. RESULTS AND DISCUSSION

The four-element MIMO antenna is designed to operate at Ka-band. The design prototype is fabricated, as shown in Figs. 16(a & b). The comprehensive antenna profile is $3.27\lambda_0 \times 3.74\lambda_0$. The |S-parameter| of the fabricated antenna is measured using KEYSIGHT VNA having a range of 300 KHz-40 GHz. The measurement setup of reflection coefficient |Sii| and transmission coefficient |Sij| (where i ≠ j) is shown in Figs. 16(c).

Capacitance C1 and C2 represent the two notches in line N1. The freely suspended lines on either side of N1 form the open circuit, which L3 and L2 represent. L6 and L7 represent lines N3 and N4; the gap between them is by capacitance C3. L8, L9, L10, and L11 imitate the rectangular stub at the center of DCS NR. The NR is a rectangular ring; capacitance
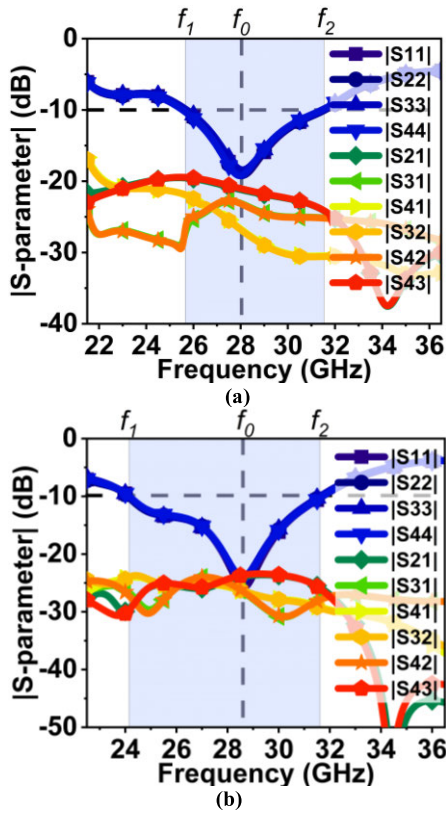
FIGURE 14. Influence of surface wave current on adjacent and opposite elements. (a) For initial DCS structure. (b) For proposed DCS structure.

A. |S-PARAMETER| ANALYSIS

The proposed MIMO antenna has resulted in a stable reflection coefficient |Sii| parameter, as shown in Fig. 14(b). The |S-parameter| of simulated and measured results are in good compliance. The simulated reflection coefficient curve from all four ports closely overlaps. The resulting bandwidth at |S11| > 10 dB is 24.10-31.72 GHz. The measured bandwidth is 24.10-30.9 GHz, as shown in Fig. 17(c). The resonance of the measured result is slightly shifted to 29.5 GHz, compared to the 28.5 GHz simulated result. The slight deviation in measured results is due to fabrication tolerance, measurement setup, connectors, and cable losses. However, the variations are within acceptable limits. The simulated isolation |S21| is > 25 dB, whereas the measurement |S21| has resulted in > 30 dB. The simulated maximum gain is 6.7 dBi with an average of 5.8 dBi in the band of interest. The measured maximum gain is 6.5 dBi with an average of 5.31 dBi, as displayed in Fig. 17(b).

B. RADIATION PATTERN

The radiation pattern is measured in an anechoic chamber. Measurement is performed at three different frequencies, i.e., 26 GHz, 28 GHz, and 30 GHz. The simulated and measured radiation patterns are on good terms. The XZ plane has resulted in bidirectional radiation with beams tiled at approximately 334^0 and 210^0. However, the YZ plane has
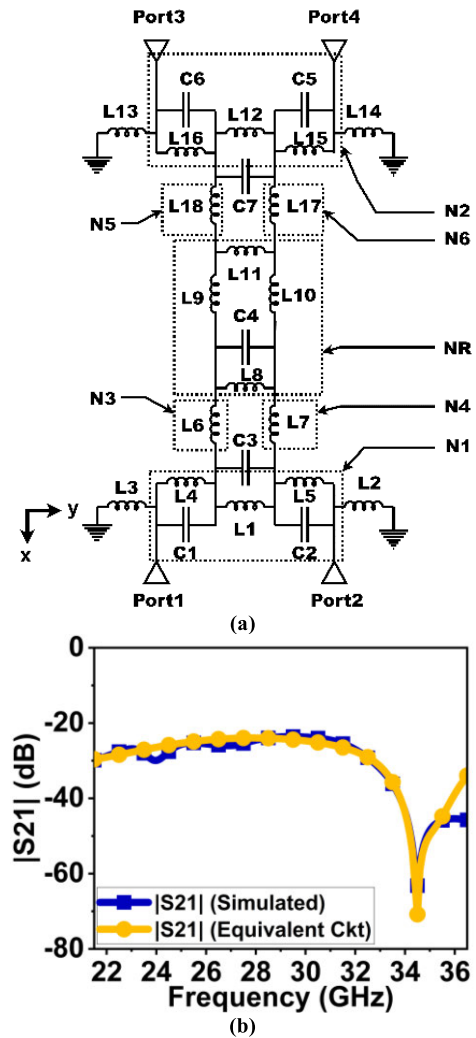

FIGURE 15. (a) LC equivalent circuit of proposed DCS structure. (b) |S21| curve generated from equivalent circuit comparable with a simulated response.

TABLE 3. LC values of DCS equivalent circuit.

Parameter	Value	Parameter	Value
C1	0.123	C2	0.052
C3	0.206	C4	0.144
C5	0.2	C6	0.060
C7	0.022	L1	0.052
L2	0.106	L3	0.662
L4	0.674	L5	0.406
L6	0.001	L7	0.360
L8	0.360	L9	0.260
L10	0.346	L11	0.020
L12	0.500	L13	0.596
L14	0.380	L15	0.750
L16	1.016	L17	0.002
L18	0.474		

Note: Inductance L is in nH, and capacitance C is in pF.

a triple beam. The reason for such a pattern is justified in the CMA analysis. The proposed design has Mode 2 as an efficient resonant mode supported partially by Modes 3 and 5. The surface current in these modes has an in-phase current in
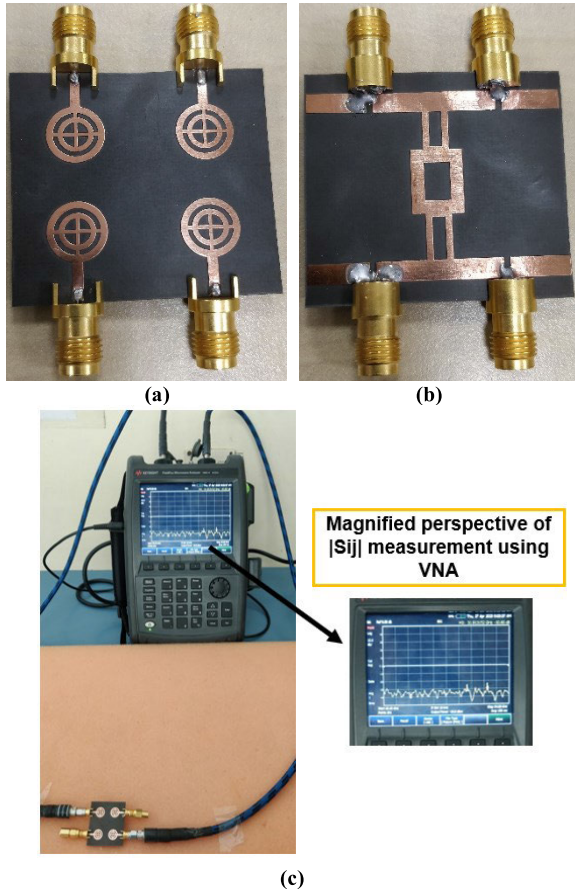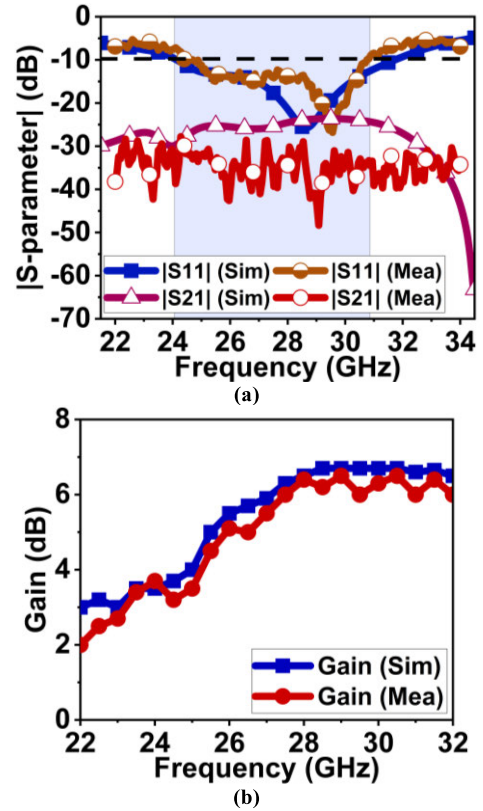
FIGURE 16. Prototype fabricated MIMO antenna and its measurement setup. (a) Top view of fabricated antenna. (b) Bottom view of fabricated antenna. (c) |Sii| and |Sij| measurement setup.

FIGURE 17. Simulated and measured results of proposed MIMO antenna. (a) |S-parameter|, (b) gain plot.

the radiator and in the ground plane. However, the in-phase current in the ground plane is at the horizontal edges, resulting in bidirectional radiation with nulls at a different angle of the azimuthal plane (Fig. 8). The designed antenna has resulted in linear polarization in both planes.

The normalized radiation patterns are shown in Fig. 18. The simulated and measured half-power-beamwidth (HPBW) at 26 GHz is approximately 54^0 and 72^0, as shown in Fig. 18(a). The YZ plane beams are at 12^0, 152^0, and 225^0 angles. Its HPBW is 45^0 and 77^0, as displayed in Fig. 18(b). The simulated and measured HPBW at 28 GHz in the XZ plane is 48^0 and 60^0, as displayed in Fig. 18(c). The HPBW in the YZ plane is 40^0 and 50^0, respectively, in Fig. 18(d). At 30 GHz, XZ plane HPBW is 40^0 and 44^0, in Fig. 18(e). The HPBW at the YZ plane is 35^0 and 55^0, simulated and measured in Fig. 18(f).

C. DIVERSITY PERFORMANCE

The MIMO antenna designed for wireless communication systems should be legitimized with the diversity metrics. The envelope correlation coefficient (ECC) indicates the correlation of received signals between MIMO antennas. It is calculated from the radiation pattern using the equation

defined in [15]. The acceptable value of ECC < 0.5. The proposed antenna resulted in ECC < 0.18 in Fig. 19(a). The diversity gain (DG) reveals the MIMO systems signal-to-noise (SNR) ratio improvement. It depends on the correlation of signals received at multiple antennas. When the received signals are uncorrelated, it means ECC = 0. Then, the DG is calculated as $\sqrt{1 - ECC^2}$ which results in 10 [37]. Ideally, the DG value of 10 indicates a good MIMO system. The proposed MIMO antenna has a DG value close to 10 in Fig. 19(b). The channel capacity loss (CCL) represents the transmission loss in terms of bit-error rate (BER). It is calculated using the equations presented in [33]. The acceptable value of CCL < 0.4 b/s/Hz. For the proposed MIMO antenna, CCL < 0.25 b/s/Hz, as depicted in Fig. 19(c). The total active reflection coefficient (TARC) measures the MIMO antenna efficiency by considering reflection losses calculated from the equations mentioned in [38]. TARC value must be greater than 10 dB for the region of interest. The proposed MIMO antenna satisfies the required condition in Fig. 26(d). The mean effective gain (MEG) measures the MIMO antenna effective gain by considering the spatial characteristics and MIMO antenna correlation. It is calculated using equations provided in [39]. Ideally, it should be < 3 dB, and the ratio must result in zero. The results in Fig. 19(e) satisfy the MEG requirement.
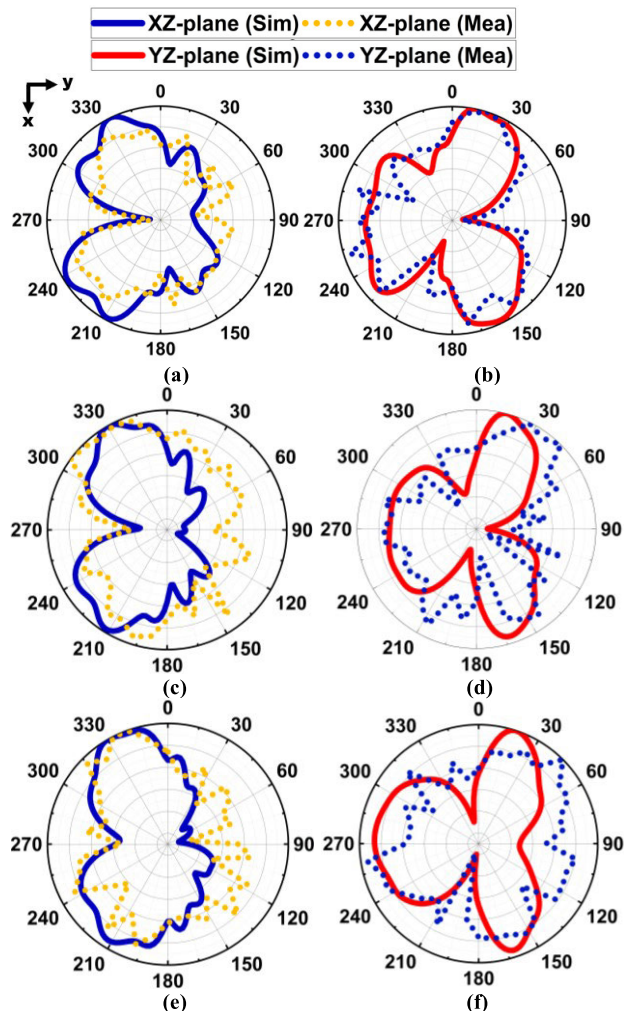
FIGURE 18. Normalized simulated and measured radiation pattern at three different frequencies in the band of interest. (a & b) XZ & YZ plane at 26 GHz, (c & d) XZ & YZ plane at 28 GHz, (e & f) XZ & YZ plane at 30 GHz.

V. SCALABILITY OF PROPOSED ANTENNA

To check the scalability of the designed antenna, it is expanded to a six-element MIMO antenna to demonstrate the possibility of n-element MIMO expansion. In addition to the four-elements, two other vertically mirrored elements, fifth and sixth, are symmetrically extended along the y-axis, as shown in Fig. 20(a) to form the six element antenna. The ground structure below these elements is replicated with partial ground like the four element antenna. The decoupling design consisting of three rectangular rings between ports 1, 2, 3, and 4 are reproduced between ports 2, 4, 5, and 6, as indicated in Fig. 20(b). The chosen substrate length is $TSS_L = 35$ mm, and the width is $TSS_W = 60$ mm. Therefore, the overall antenna profile is $3.27\lambda_0 \times 5.6\lambda_0$.

Here, the purpose is to show the scalability of the proposed four element MIMO antenna so, only the simulated |S-parameter| results and its corresponding surface current distribution of the six-element MIMO antenna is presented. The resulting reflection coefficient in Fig. 21(a) indicates that all the elements resonate at 28.5 GHz with a slight deviation
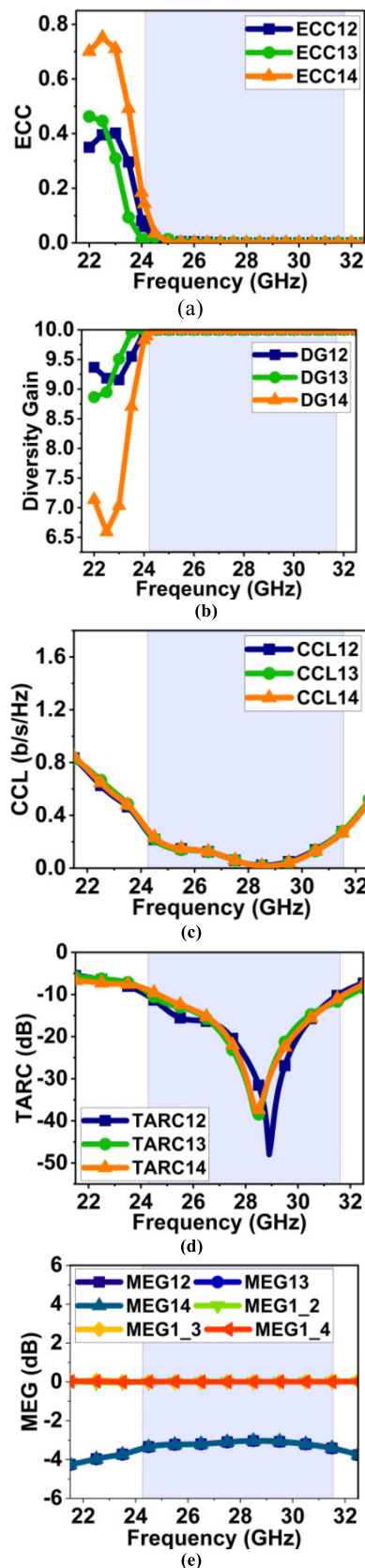
FIGURE 19. Diversity performance of proposed MIMO antenna. (a) Envelope correlation coefficient (ECC), (b) diversity gain (DG), (c) channel capacity loss (CCL), (d) total active reflection coefficient (TARC), and (e) mean effective gain graphs.

as compared to the proposed four element MIMO antenna. The antenna element of ports 1, 3, 5, and 6 has an open circuit on one end and DCS at the other end of the ground plane.
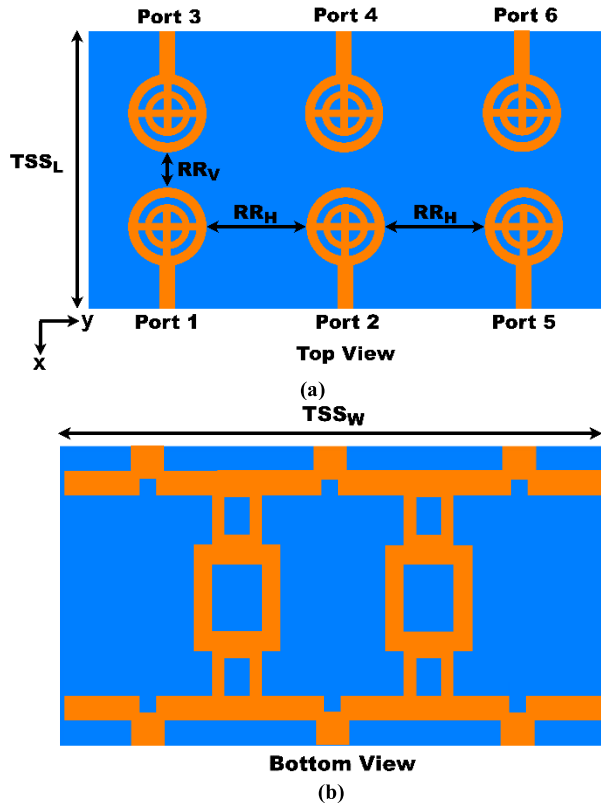

FIGURE 20. Extension of four-element MIMO to six-element MIMO antenna. (a) Top view, (b) bottom view.

FIGURE 21. |S-parameter| of six-element MIMO antenna. (a) Reflection coefficient |Sii|, (b) Isolation |Sij|.
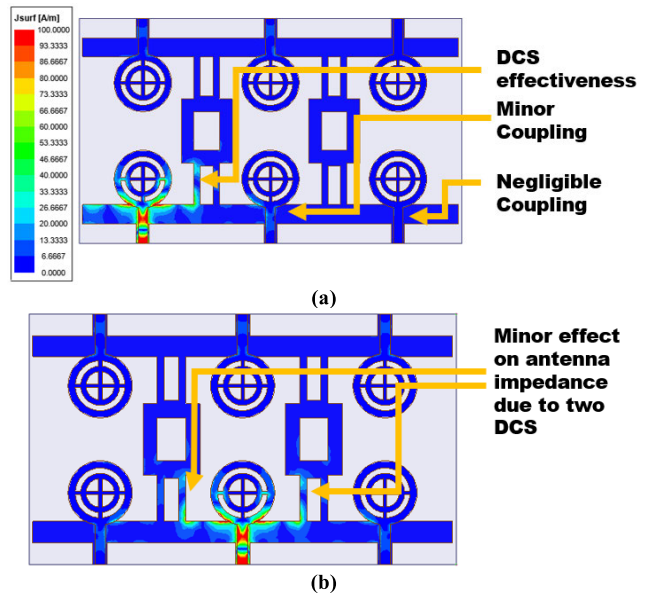
FIGURE 22. Surface wave distribution of six-element MIMO antenna. (a) When port 1 is excited. (b) When port 2 is excited.

This setup has a minimal surface wave coupling effect (Fig. 22(a)) on the vertically mirrored elements, resulting in a good impedance matching of 27 dB. In the case of port elements 2 and 4, they lie between two DCS structures. Due to this, it reduces the coupling to adjacent elements; however, the surface waves are guided to the vertically mirrored elements. The surface wave distribution in Fig. 22(b) illustrates this phenomenon. It impacts the antenna performance in terms of impedance matching, slightly decreasing |S22| and |S44| to 20.5 dB. Also, the isolation |S42| is 23 dB in Fig. 21(b). These variations are within acceptable limits. However, the bandwidth of all the port elements has resulted in 23.5-31.72 GHz. A slight decrease in the lower frequency f_1 is observed, which has increased the bandwidth. The six-element MIMO antenna is able to maintain good isolation |Sij| > 23 dB due to the antenna geometry and proposed decoupling structure.

VI. VALIDATION OF THE PROPOSED ANTENNA IN COMMUNICATION SCENARIO

A. CHANNEL CAPACITY
The MIMO technology is being significantly employed in the field of communication to enhance the data rate
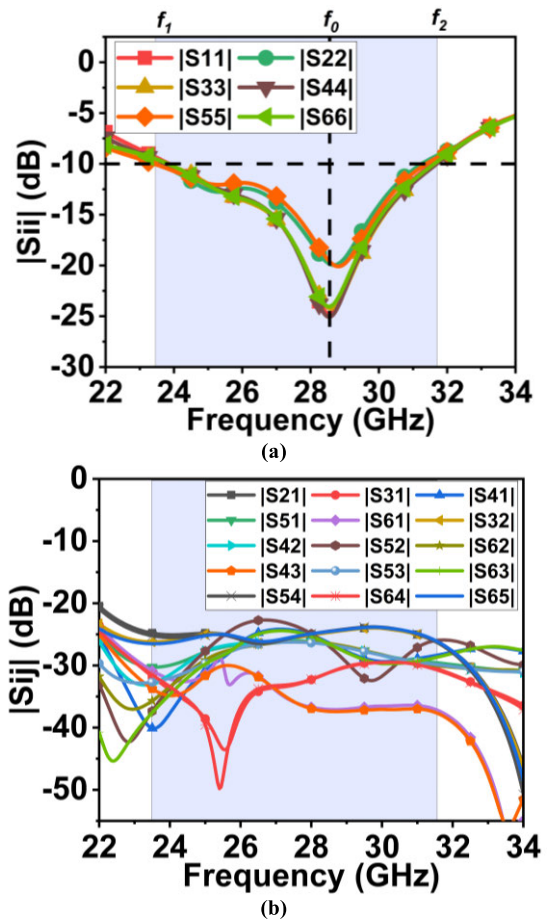
and signal-to-noise ratio (SNR) performance through spatial multiplexing and diversity techniques. However, the true performance of MIMO depends on the channel condition

and nature of the environment [35]. The channel capacity is directly related to a number of transmitting (TX) and receiving (RX) MIMO antenna, as defined in equation (2). Therefore, the channel capacity of the proposed four-element MIMO antenna is compared with Single-Input-Single-Output (SISO), MIMO with 2 TX and 2 RX, MIMO with 3 TX and 3 RX, and proposed MIMO with 4 Tx and 4 RX antenna. The performance of the MIMO antenna increases with the increase in SNR, as displayed in Fig. 23. At an SNR of 20 dB, SISO has a capacity of 5.3 Gbps. In contrast, the proposed MIMO has 10.35 Gbps, double the SISO capacity. For these calculations, the considered bandwidth is 6.8 GHz from the proposed antenna.
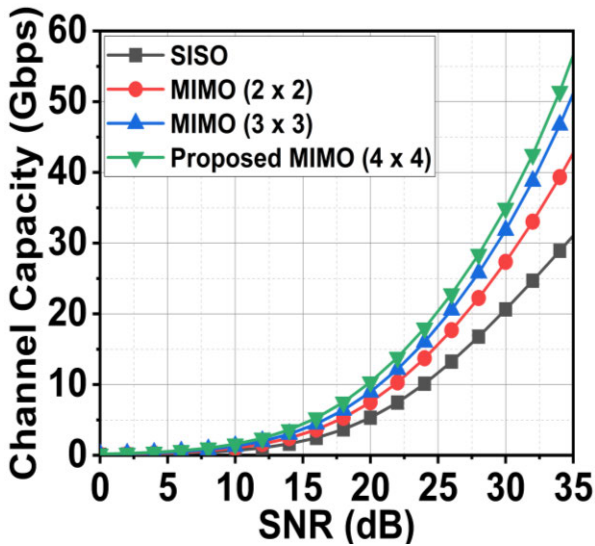

FIGURE 23. Comparison of SISO and MIMO antenna channel capacity over varied SNR.

B. PATH LOSS AND LINK MARGIN

The signal attenuation is much higher at millimeter waves, so the duplex communication between the TX and RX suffers significantly. Many factors influence the attenuation; one such factor is path loss exponent (PLE). The atmospheric conditions and signal absorption by objects in densely packed urban areas also contribute to signal attenuation [40], [41]. Therefore, the performance of the designed antenna is tested in a free space virtual line-of-sight (LOS) environment, as shown in Fig. 24. In the test scenario, the TX antenna is held stationary, and the RX antenna continuously displaced from 100 cm to 50 m, to study the path loss and link budget requirement.

The virtual environment setup analyzes and provides the received signal (P_r) considering PLE in account and other multipath effects. From this, the path loss is calculated by considering the transmitting power (P_t) and gain of the transmitting (GTX) and receiving (GRX) (measured maximum gain) antenna using (3).

$$PL\,(dB) = P_t\,(dB) - P_r(dB) + GTX\,(dB) + GRX\,(dB) \tag{3}$$
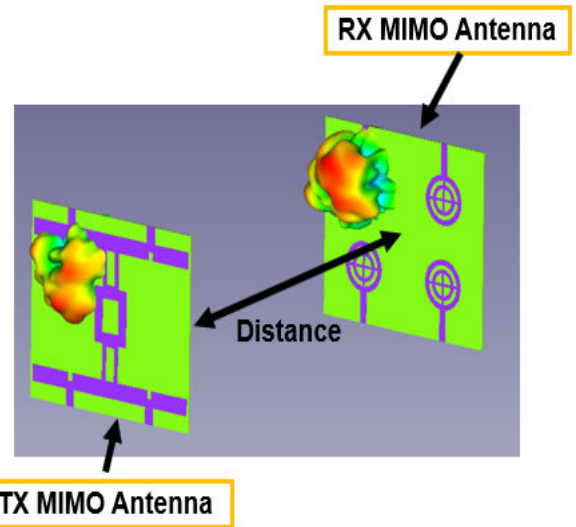

FIGURE 24. Virtual LOS environment demonstrating the path loss and link budget estimation for a communication system.

The results of calculated received power are compared with Friss free-space path loss, which is calculated using (4) [42].

$$PL_{FS}\,(dB) = -10log_{10}\left(\frac{GTX.GRX.\lambda_0^2}{(4\pi d)^2}\right) \tag{4}$$

where d is the distance in m, and λ_0 is wavelength in free space at 28 GHz.

In Fig. 25, calculated results indicate that the proposed antenna has a significant path loss of 53 dB to 75 dB for the first 1m distance, which is true at millimeter wave [42]. Further, it gradually decreases from 80 dB up to 113 dB. The free-space path loss shows a similar path loss effect but with lesser attenuation. Therefore, the Friss free-space path loss model is modified by adding the slope correction factor (α_{LOS}) and shadowing effect (X_σ) defined in (5).

$$PL_{FS\_Mod}\,(dB) = \alpha_{LOS} \times (PL_{FS} - PL_{FS}\,(1m))$$
$$+ PL\,(1m) + X_\sigma \tag{5}$$

$$PL\,(1m)\,(dB) = 20log_{10}\left(\frac{4\pi f}{c}\right) \tag{5a}$$

where $c = 3 \times 10^8$. For LOS condition, the α_{LOS} is considered as 1.25 and σ as 3.5. The modified Friss equation estimates the path loss close to the virtually simulated results in Fig. 24.

Assuming the minimum required link margin is 20 dB for reliable communication, the required power can be calculated using (6) [43].

$$RP_r\,(W) = \frac{E_b}{N_0} + KT + B_r \tag{6}$$

Here, E_b defines the energy required to transmit one bit of information over the noise N_0, where noise is power

TABLE 4. Structural analysis of proposed MIMO antenna with existing state-of-art.

| Ref.	MIMO Antenna Desing Techniques	Method to Enhance Isolation	Scalability Feature	Link Budget Analysis	Complexity of the Design	Radiation Performance
[14]	Orthogonal with connected ground	Corrugated ground plane	No	No	Easy	Broadside with back radiation
[15]	Orthogonal with disconnected ground	Partial + Disconnected ground	No	No	Complex	Non-uniform Omnidirectinal
[16]	Orthogonal with connected ground	Self-regulating structure	No	No	Complex	Broadside with wide beamwidth
[17]	Diagonal with connected ground	Tapered ground + Large separation	No	No	Complex	Broadside at different angles of θ and φ
[18]	Symmetrical with connected ground	Defected ground + Large separation	Yes	No	Complex	Broadside with back radiation
[19]	Orthogonal with connected ground	DCS on top + slots in ground	No	No	Complex	Broadside with wide beam
[20]	Orthogonal with disconnected ground	Disconnected ground	No	No	Easy	Bidirectional
[21]	Orthogonal with disconnected ground	Partial and disconnected ground	No	No	Complex	Omnidirectional
[22]	Orthogonal with disconnected ground	Fan shape DCS on top + partial and disconnected ground	No	No	Complex	Bidirectional /omnidirectional
[23]	Orthogonal with connected ground	DCS + Defected ground	No	No	Complex	Broadside with tilted beam
[44]	Symmetrical with disconnected ground	Disconnected + Defected and partial ground	Yes	No	Complex	Bidirectional
[45]	Orthogonal with disconnected ground	Disconnect + Partial ground	No	No	Easy	NA
[46]	Orthogonal with connected ground	Slot based	No	No	Easy	Broadside
Proposed MIMO	Symmetrical with connected ground	DCS + Partial ground	Yes	Yes	Complex	Bidirectional
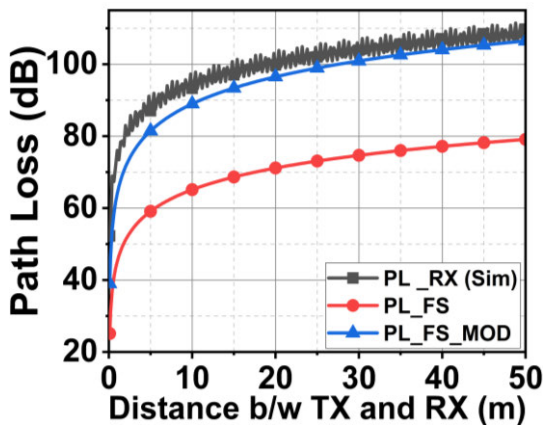
FIGURE 25. Calculated path loss of proposed MIMO antenna and compared with existing path loss models.

spectral density. The ideal BPSK with Eb/N0 of 9.6 dB is assumed. The K is the Boltzmann constant, and T is the temperature in kelvin, which is 290. The B_r is the bit rate supported for communication with a minimum link margin.

The link margin is given by (7):

$$Link\ Margin\ (LM)\ (dB) = P_r - RP_r \qquad (7)$$

Fig. 26 illustrates the link margin for the proposed MIMO antenna over varied bit rates. It indicates that at LM of 20 dB, 20 Gbps data rate is supported only up to 5 meters of distance. However, for a reduced data rate of 2 Gbps, the distance is increased to 10 m. Further, a 1 Gbps data rate is supported to a maximum of 15 m. On the other side, with a reduced data rate to 100 Mbps, the proposed antenna supports up to a distance of 40 m.

VII. COMPARATIVE ANALYSIS

This section presents the structural and performance comparison of the proposed MIMO antenna with the existing designs, as listed in Tables 3 and 4. Most antenna structures listed in these tables have orthogonal arrangements except [18] and [44]. These types of structures are basic methods to design MIMO antenna, which naturally provide good isolation but lack in terms of scalability. Also, all the compared articles do not provide any power performance information for the defined structure. However, the proposed

TABLE 5. Performance of proposed MIMO antenna with existing state-of-art.

Ref.	Dim (λ_0 is calculated @ Res)s	Ports	Res (GHz)	BW (GHz)	Iso (dB)	Gain (dBi)	GD	ECC	DG	CCL (b/s/Hz)	TARC (dB)	MEG (dB)
[14]	$2.85\lambda_0 \times 2.85\lambda_0$	04	28	26.5-29.5	> 31	7	Con	< 0.0005	NA	< 0.15	NA	NA
[15]	$2.85\lambda_0 \times 2.85\lambda_0$	04	28	27.2-29.2	> 29	6.1	Dis	< 0.16	NA	NA	NA	> 3
[16]	$7.47\lambda_0 \times 7.47\lambda_0$	04	28	24-38	> 20	10.5	Con	< 0.0014	NA	NA	NA	> 5
[17]	$9.47\lambda_0 \times 9.47\lambda_0$	04	27	22-30	> 22	10.5	Con	< 0.16	NA	NA	NA	NA
[18]	$10.3\lambda_0 \times 7\lambda_0$	04	28	26-30	> 22	9.4	Con	< 0.005	> 9.85	< 0.3	NA	> 6
[19]	$2.81\lambda_0 \times 3.27\lambda_0$	04	28	27.5-28.5	> 35	10.9	Con	< 0.0012	> 9.9	< 0.8	NA	NA
[20]	$1.87\lambda_0 \times 1.87\lambda_0$	04	28	26.5-31	> 17.5	9.2	Dis	< 0.0013	NA	NA	NA	NA
[21]	$2.33\lambda_0 \times 1.4\lambda_0$	04	28	27-29	> 17	7.8	Dis	< 0.0012	10	NA	NA	> 3
[22]	$2.25\lambda_0 \times 2.24\lambda_0$	04	28	24-39	> 21	6.4	Dis	< 0.05	NA	NA	NA	> 3
[23]	$2.91\lambda_0 \times 3.39\lambda_0$	04	29	26.2-29.5	> 10	8.1	Con	< 0.03	> 9.975	< 0.4	NA	> 7
[44]	$3.74\lambda_0 \times 1.13\lambda_0$	04	28/38	23-33 /37.75-41	> 20	5.7	Dis	< 0.00015	> 9.98	NA	NA	> 3
[45]	$3.1\lambda_0 \times 3.1\lambda_0$	04	28	25-50	> 13	NA	Dis	< 0.0015	> 9.99	< 0.25	< 10	NA
[46]	$3.55\lambda_0 \times 3.37\lambda_0$	04	28	27.2-29	> 23	7.5	Con	< 0.002	> 9.99	NA	NA	NA
Proposed MIMO	$3.27\lambda_0 \times 3.74\lambda_0$	04	28	24.1-30.9	> 30	6.5	Con	< 0.18	10	< 0.25	< 10	> 3

Note: Ref – Reference, Dim – Dimension, Res-Resonance, BW - Bandwidth, Iso – Isolation, Gain – Peaks gain, GD – Ground, Con – Connected ground, Dis – Disconnected ground, NA – Not available.
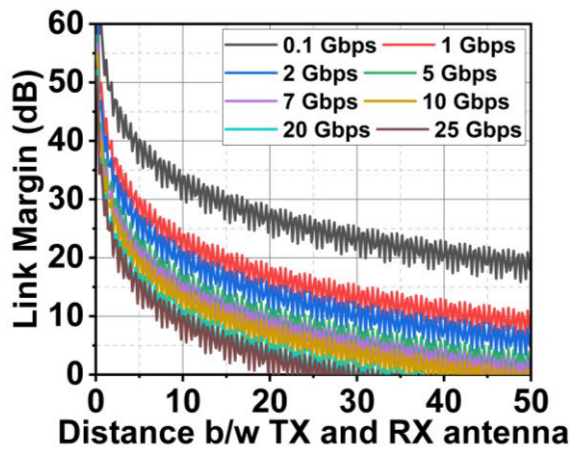

FIGURE 26. Calculated link margin of proposed MIMO over varied bit rates.

antenna has the ability to scale for n-element MIMO. The antenna is also analyzed for channel capacity and link budget calculation. As discussed in the introduction section, a MIMO antenna must have a common ground for a voltage reference point, which most of the designs, such as [15], [20], [21], [22], [44], and [45], failed to address. The proposed antenna addresses the above issue with connected ground through a novel DCS structure. The proposed antenna has resulted in a stable |S-parameter| response with an isolation of > 30 dB, which is better than [16], [17], [18], [20], [21], [23], [44],

[45], and [46]. The designed antenna has wide bandwidth compared to [14], [15], [18], [19], [20], [21], and [23]. Most of the antenna in the literature, such as [14], [16], [18], [19], [20], [21], [44], [45], and [46], has computed the ECC using |S-parameter|, which is an approximate and inaccurate method. The correct ECC is calculated through a radiation pattern by considering all the radiation losses. The proposed antenna ECC is measured using radiation pattern method, which resulted in < 0.18 (well below the acceptable limit). Also, in the compared article, none of them analyze the full diversity parameters. However for the proposed antenna all the diversity performance have been analyzed and it is better as compared to those presented in the literature at millimeter wave frequency, as shown in Table 5.

VIII. CONCLUSION

This article presented a stable wideband four-element MIMO antenna operating at Ka-band. The configuration of MIMO is such that it can be expanded to an n-element MIMO antenna. The characteristics mode theory clarifies the behavior of the antenna structure and mode excitations. Mode 2 is an efficient and dominant mode with minor contributing modes 3 and 5. Also, the surface current distribution and radiation pattern behavior are analyzed using CMA. Further, the article also proposed a novel decoupling structure in the ground plane, which helps in achieving good isolation of 30 dB. The reflection coefficient |Sii| response of all port elements has produced similar results with negligible distortion. The article also presented the analyses of the DCS equivalent circuit

whose |S-parameter| response closely matches the proposed antenna. The antenna has resulted in a stable radiation pattern over the entire band with a maximum gain of 6.5 dBi. The article also demonstrated the possibility of expanding the MIMO antenna to an n-element through a six-element MIMO antenna design. The path loss of the proposed MIMO antenna shows that in an LOS condition, it has a loss of 113 dB for a distance of 50 m. The proposed antenna can support 1 Gbps of data to a distance of 15-20 m for a link margin of 20 dB. Also, the proposed MIMO antenna satisfies all the diversity metrics and is thus suitable for millimeter-wave 5G wireless applications.

REFERENCES

[1] N. K. Mallat, M. Ishtiaq, A. U. Rehman, and A. Iqbal, "Millimeter-wave in the face of 5G communication potential applications," *IETE J. Res.*, vol. 68, no. 4, pp. 2522–2530, Jul. 2022, doi: 10.1080/03772063.2020.1714489.

[2] P. R. Mane, P. Kumar, T. Ali, and M. G. N. Alsath, "Planar MIMO antenna for mmWave applications: Evolution, present status & future scope," *Heliyon*, vol. 9, no. 2, Feb. 2023, Art. no. e13362, doi: 10.1016/j.heliyon.2023.e13362.

[3] A. F. Molisch and M. Z. Win, "MIMO systems with antenna selection," *IEEE Microw. Mag.*, vol. 5, no. 1, pp. 46–56, Mar. 2004, doi: 10.1109/MMW.2004.1284943.

[4] M. Ikram, N. Nguyen-Trong, and A. M. Abbosh, "Realization of a tapered slot array as both decoupling and radiating structure for 4G/5G wireless devices," *IEEE Access*, vol. 7, pp. 159112–159118, 2019, doi: 10.1109/ACCESS.2019.2950660.

[5] A. Kumar, A. Q. Ansari, B. K. Kanaujia, and J. Kishor, "A novel ITI-shaped isolation structure placed between two-port CPW-fed dual-band MIMO antenna for high isolation," *AEU-Int. J. Electron. Commun.*, vol. 104, pp. 35–43, May 2019, doi: 10.1016/j.aeue.2019.03.009.

[6] A. Ahmad, D.-Y. Choi, and S. Ullah, "A compact two elements MIMO antenna for 5G communication," *Sci. Rep.*, vol. 12, no. 1, p. 3608, Mar. 2022, doi: 10.1038/s41598-022-07579-5.

[7] Z. Wang, C. Li, Q. Wu, and Y. Yin, "A metasurface-based low-profile array decoupling technology to enhance isolation in MIMO antenna systems," *IEEE Access*, vol. 8, pp. 125565–125575, 2020, doi: 10.1109/ACCESS.2020.3007188.

[8] M. Alibakhshikenari, F. Babaeian, B. S. Virdee, S. Aïssa, L. Azpilicueta, C. H. See, A. A. Althuwayb, I. Huynen, R. A. Abd-Alhameed, F. Falcone, and E. Limiti, "A comprehensive survey on 'various decoupling mechanisms with focus on metamaterial and metasurface principles applicable to SAR and MIMO antenna systems,'" *IEEE Access*, vol. 8, pp. 192965–193004, 2020, doi: 10.1109/ACCESS.2020.3032826.

[9] N. Hussain, W. A. Awan, W. Ali, S. I. Naqvi, A. Zaidi, and T. T. Le, "Compact wideband patch antenna and its MIMO configuration for 28 GHz applications," *AEU-Int. J. Electron. Commun.*, vol. 132, Apr. 2021, Art. no. 153612, doi: 10.1016/j.aeue.2021.153612.

[10] H. Zahra, W. A. Awan, W. A. E. Ali, N. Hussain, S. M. Abbas, and S. Mukhopadhyay, "A 28 GHz broadband helical inspired end-fire antenna and its MIMO configuration for 5G pattern diversity applications," *Electronics*, vol. 10, no. 4, p. 405, Feb. 2021, doi: 10.3390/electronics10040405.

[11] D. E. Hadri, A. Zakriti, A. Zugari, M. E. Ouahabi, and J. E. Aoufi, "High isolation and ideal correlation using spatial diversity in a compact MIMO antenna for fifth-generation applications," *Int. J. Antennas Propag.*, vol. 2020, pp. 1–10, Jul. 2020, doi: 10.1155/2020/2740920.

[12] F. Taher, H. A. Hamadi, M. S. Alzaidi, H. Alhumyani, D. H. Elkamchouchi, Y. H. Elkamshoushy, M. T. Haweel, M. F. A. Sree, and S. Y. A. Fatah, "Design and analysis of circular polarized two-port MIMO antennas with various antenna element orientations," *Micromachines*, vol. 14, no. 2, p. 380, Feb. 2023, doi: 10.3390/mi14020380.

[13] B. T. P. Madhav, Y. Usha Devi, and T. Anilkumar, "Defected ground structured compact MIMO antenna with low mutual coupling for automotive communications," *Microw. Opt. Technol. Lett.*, vol. 61, no. 3, pp. 794–800, Mar. 2019, doi: 10.1002/mop.31626.

[14] M. Hussain, E. Mousa Ali, S. M. R. Jarchavi, A. Zaidi, A. I. Najam, A. A. Alotaibi, A. Althobaiti, and S. S. M. Ghoneim, "Design and characterization of compact broadband antenna and its MIMO configuration for 28 GHz 5G applications," *Electronics*, vol. 11, no. 4, p. 523, Feb. 2022, doi: 10.3390/electronics11040523.

[15] M. M. Kamal, S. Yang, X.-C. Ren, A. Altaf, S. H. Kiani, M. R. Anjum, A. Iqbal, M. Asif, and S. I. Saeed, "Infinity shell shaped MIMO antenna array for mm-wave 5G applications," *Electronics*, vol. 10, no. 2, p. 165, Jan. 2021, doi: 10.3390/electronics10020165.

[16] D. A. Sehrai, M. Abdullah, A. Altaf, S. H. Kiani, F. Muhammad, M. Tufail, M. Irfan, A. Glowacz, and S. Rahman, "A novel high gain wideband MIMO antenna for 5G millimeter wave applications," *Electronics*, vol. 9, no. 6, p. 1031, Jun. 2020, doi: 10.3390/electronics9061031.

[17] M. Ikram, N. Nguyen-Trong, and A. Abbosh, "Multiband MIMO microwave and millimeter antenna system employing dual-function tapered slot structure," *IEEE Trans. Antennas Propag.*, vol. 67, no. 8, pp. 5705–5710, Aug. 2019, doi: 10.1109/TAP.2019.2922547.

[18] S. Iffat Naqvi, N. Hussain, A. Iqbal, M. Rahman, M. Forsat, S. S. Mirjavadi, and Y. Amin, "Integrated LTE and millimeter-wave 5G MIMO antenna system for 4G/5G wireless terminals," *Sensors*, vol. 20, no. 14, p. 3926, Jul. 2020, doi: 10.3390/s20143926.

[19] M. Bilal, S. I. Naqvi, N. Hussain, Y. Amin, and N. Kim, "High-isolation MIMO antenna for 5G millimeter-wave communication systems," *Electronics*, vol. 11, no. 6, p. 962, Mar. 2022, doi: 10.3390/electronics11060962.

[20] S. Sharma and M. Arora, "A millimeter wave elliptical slot circular patch MIMO antenna for future 5G mobile communication networks," *Prog. Electromagn. Res. M*, vol. 110, p. 13, 2022.

[21] S. Rahman, X.-C. Ren, A. Altaf, M. Irfan, M. Abdullah, F. Muhammad, M. R. Anjum, S. N. F. Mursal, and F. S. AlKahtani, "Nature inspired MIMO antenna system for future mmWave technologies," *Micromachines*, vol. 11, no. 12, p. 1083, Dec. 2020, doi: 10.3390/mi11121083.

[22] M. A. Khan, A. G. Al Harbi, S. H. Kiani, A. N. Nordin, M. E. Munir, S. I. Saeed, J. Iqbal, E. M. Ali, M. Alibakhshikenari, and M. Dalarsson, "mmWave four-element MIMO antenna for future 5G systems," *Appl. Sci.*, vol. 12, no. 9, p. 4280, Apr. 2022, doi: 10.3390/app12094280.

[23] M. Khalid, S. I. Naqvi, N. Hussain, M. Rahman, S. S. Mirjavadi, M. J. Khan, and Y. Amin, "4-port MIMO antenna with defected ground structure for 5G millimeter wave applications," *Electronics*, vol. 9, no. 1, p. 71, Jan. 2020, doi: 10.3390/electronics9010071.

[24] M. S. Sharawi, "Current misuses and future prospects for printed multiple-input, multiple-output antenna systems [wireless corner]," *IEEE Antennas Propag. Mag.*, vol. 59, no. 2, pp. 162–170, Apr. 2017, doi: 10.1109/MAP.2017.2658346.

[25] C. A. Balanis, *Antenna Theory: Analysis and Design*, 4th ed. Hoboken, NJ, USA: Wiley, 2016.

[26] M. Xue, W. Wan, Q. Wang, and L. Cao, "Low-profile millimeter-wave broadband metasurface antenna with four resonances," *IEEE Antennas Wireless Propag. Lett.*, vol. 20, no. 4, pp. 463–467, Apr. 2021, doi: 10.1109/LAWP.2021.3053589.

[27] Z. Xu and Y. Wang, "Design of dual-band antenna for metal-bezel smartwatches with circular-polarization in GPS band and low wrist effect," *IEEE Trans. Antennas Propag.*, vol. 71, no. 6, pp. 4651–4662, Jun. 2023, doi: 10.1109/TAP.2023.3256582.

[28] M. Khan and D. Chatterjee, "Characteristic mode analysis of a class of empirical design techniques for probe-fed, U-slot microstrip patch antennas," *IEEE Trans. Antennas Propag.*, vol. 64, no. 7, pp. 2758–2770, Jul. 2016, doi: 10.1109/TAP.2016.2556705.

[29] G. Gao, R.-F. Zhang, W.-F. Geng, H.-J. Meng, and B. Hu, "Characteristic mode analysis of a nonuniform metasurface antenna for wearable applications," *IEEE Antennas Wireless Propag. Lett.*, vol. 19, no. 8, pp. 1355–1359, Aug. 2020, doi: 10.1109/LAWP.2020.3001049.

[30] T. Li and Z. N. Chen, "A dual-band metasurface antenna using characteristic mode analysis," *IEEE Trans. Antennas Propag.*, vol. 66, no. 10, pp. 5620–5624, Oct. 2018, doi: 10.1109/TAP.2018.2860121.

[31] M. Vogel, G. Gampala, D. Ludick, U. Jakobus, and C. J. Reddy, "Characteristic mode analysis: Putting physics back into simulation," *IEEE Antennas Propag. Mag.*, vol. 57, no. 2, pp. 307–317, Apr. 2015, doi: 10.1109/MAP.2015.2414670.

[32] A. Mohanty and B. R. Behera, "Characteristics mode analysis: A review of its concepts, recent trends, state-of-the-art developments and its interpretation with a fractal UWB MIMO antenna," *Prog. Electromagn. Res. B*, vol. 92, pp. 19–45, 2021, doi: 10.2528/PIERB21020506.

[33] M. Sharma, T. Addepalli, R. Manda, T. Vidyavathi, and P. R. Kapula, "A detailed insight of 2 × 2 high isolation wideband dual notched band MIMO antenna with evolution initiated by theory of characteristics mode," *Int. J. Microw. Wireless Technol.*, vol. 2023, pp. 1–20, Feb. 2023, doi: 10.1017/S1759078723000028.

[34] A. Mohanty and B. R. Behera, "CMA assisted 4-port compact MIMO antenna with dual-polarization characteristics," *AEU-Int. J. Electron. Commun.*, vol. 137, Jul. 2021, Art. no. 153794, doi: 10.1016/j.aeue.2021.153794.

[35] R. Ahmad, D. Pratap Singh, and M. Singh, "Ergodic capacity of MIMO channel in multipath fading environment," *Int. J. Inf. Eng. Electron. Bus.*, vol. 5, no. 3, pp. 41–48, Sep. 2013, doi: 10.5815/ijieeb.2013.03.05.

[36] A. Sharma, A. Sarkar, A. Biswas, and M. J. Akhtar, "Dual-band multiple-input multiple-output antenna based on half split cylindrical dielectric resonator," *J. Electromagn. Waves Appl.*, vol. 32, no. 9, pp. 1152–1163, Jun. 2018, doi: 10.1080/09205071.2018.1425159.

[37] T. Addepalli, M. S. Kumar, V. S. Nagaraju, M. Sharma, and P. R. Kapula, "Compact 4-port wideband MIMO antenna with connected ground, high diversity performance and dual-notched filters," *IETE J. Res.*, vol. 2023, pp. 1–22, Aug. 2023, doi: 10.1080/03772063.2023.2245379.

[38] A. Khabba, J. Amadid, S. Ibnyaich, and A. Zeroual, "Pretty-small four-port dual-wideband 28/38 GHz MIMO antenna with robust isolation and high diversity performance for millimeter-wave 5G wireless systems," *Anal. Integr. Circuits Signal Process.*, vol. 112, no. 1, pp. 83–102, Jul. 2022, doi: 10.1007/s10470-022-02045-8.

[39] S. S. Bhatia and N. Sharma, "Modified spokes wheel shaped MIMO antenna system for multiband and future 5G applications: Design and measurement," *Prog. Electromagn. Res. C*, vol. 117, pp. 261–276, 2021, doi: 10.2528/PIERC21111102.

[40] N. Hosseini, M. Khatun, C. Guo, K. Du, O. Ozdemir, D. W. Matolak, I. Guvenc, and H. Mehrpouyan, "Attenuation of several common building materials: Millimeter-wave frequency bands 28, 73, and 91 GHz," *IEEE Antennas Propag. Mag.*, vol. 63, no. 6, pp. 40–50, Dec. 2021, doi: 10.1109/MAP.2020.3043445.

[41] I. A. Hemadeh, K. Satyanarayana, M. El-Hajjar, and L. Hanzo, "Millimeter-wave communications: Physical channel models, design considerations, antenna constructions, and link-budget," *IEEE Commun. Surveys Tuts.*, vol. 20, no. 2, pp. 870–913, 2nd Quart., 2018, doi: 10.1109/COMST.2017.2783541.

[42] A. I. Sulyman, A. Alwarafy, G. R. MacCartney, T. S. Rappaport, and A. Alsanie, "Directional radio propagation path loss models for millimeter-wave wireless networks in the 28-, 60-, and 73-GHz bands," *IEEE Trans. Wireless Commun.*, vol. 15, no. 10, pp. 6939–6947, Oct. 2016, doi: 10.1109/TWC.2016.2594067.

[43] A. Iqbal, M. Al-Hasan, I. B. Mabrouk, and M. Nedil, "Scalp-implantable MIMO antenna for high-data-rate head implants," *IEEE Antennas Wireless Propag. Lett.*, vol. 20, no. 12, pp. 2529–2533, Dec. 2021, doi: 10.1109/LAWP.2021.3117345.

[44] M. E. Munir, S. H. Kiani, H. S. Savci, M. Marey, J. Khan, H. Mostafa, and N. O. Parchin, "A four element mm-wave MIMO antenna system with wide-band and high isolation characteristics for 5G applications," *Micromachines*, vol. 14, no. 4, p. 776, Mar. 2023, doi: 10.3390/mi14040776.

[45] M. A. Abbas, A. Allam, A. Gaafar, H. M. Elhennawy, and M. F. A. Sree, "Compact UWB MIMO antenna for 5G millimeter-wave applications," *Sensors*, vol. 23, no. 5, p. 2702, Mar. 2023, doi: 10.3390/s23052702.

[46] I. Ud Din, M. Alibakhshikenari, B. S. Virdee, R. K. R. Jayanthi, S. Ullah, S. Khan, C. H. See, L. Golunski, and S. Koziel, "Frequency-selective surface-based MIMO antenna array for 5G millimeter-wave applications," *Sensors*, vol. 23, no. 15, p. 7009, Aug. 2023, doi: 10.3390/s23157009.

AKSHAY ANIL NAIK received the B.E. degree in electronics and communication engineering from Vishveshvaraya Technological University, Belagavi, India, in 2020. He is currently pursuing the master's degree with the Department of Electronics and Communication Engineering, Manipal Institute of Technology, Manipal, India. His research interests include microstrip antennas and digital communication.

TANWEER ALI (Senior Member, IEEE) is currently an Associate Professor with the Department of Electronics and Communication Engineering, Manipal Institute of Technology, Manipal Academy of Higher Education, Manipal. He is an active researcher in the field of microstrip antennas, wireless communication, and microwave imaging. He has been listed in top 2% scientists across the world for the year 2021 and 2022, by the prestigious list published by Stanford University, USA, indexed by Scopus. He has published more than 130 papers in reputed web of science (SCI) and Scopus indexed journals and conferences. He has seven Indian patents, of which three have published. He is on the Board of a Reviewer of journals, such as IEEE Transactions on Antennas and Propagation, IEEE Antennas and Wireless Propagation Letters, IEEE Access, *IET Microwaves, Antennas and Propagation*, *IET of Electronics Letter*, *Wireless Personal Communications* (Springer), *AEU-International Journal of Electronics and Communications*, *Microwave and Optical Technology Letters* (Wiley), *International Journal of Antennas and Propagation* (Hindawi), *Advanced Electromagnetics*, *Progress in Electromagnetics Research* (PIER), *KSII Transactions on Engineering Science*, *International Journal of Microwave and Wireless Technologies*, *Frequenz*, *Radioengineering*, and IEEE Open Journal of Antennas and Propagation.

PALLAVI R. MANE (Senior Member, IEEE) received the B.E. degree in electronics and communication engineering from the Gogte Institute of Technology, India, in 1996, the M.Tech. degree in digital electronics and advanced communication from the National Institute of Technology, Surathkal, Karnataka, India, in 2002, and the Ph.D. degree in electronics and communication engineering from the Manipal Institute of Technology, MAHE, Manipal, in 2014, for the thesis in network coding. She is currently a Professor with the Department of ECE, MIT-MAHE. She has authored several papers in international conferences and journal proceedings. Her research interests include network coding, source, and channel coding, and communication engineering.

PARVEEZ SHARIFF B. G. (Student Member, IEEE) received the B.E. degree in telecommunication engineering and the M.Tech. degree in digital electronics and communication systems from Visvesvaraya Technological University, Belagavi, India, in 2007 and 2009, respectively. He is currently pursuing the Ph.D. degree in electronics and communication engineering with the Manipal Institute of Technology, Manipal, India. His research interests include microstrip antenna, array antenna, flexible antenna, and metamaterial structure. He is a LMISTE Member in India.

RAJIV MOHAN DAVID received the B.E. degree (Hons.) in electronics and communication engineering from Bharathiar University, in April 1998, the M.B.A. degree (Hons.) from the University of Madras, in April 2000, the M.E. degree (Hons.) in applied electronics from Bharathiar University, in December 2001, and the Ph.D. degree from the Manipal Institute of Technology, MAHE, Manipal. He is currently an Associate Professor with the Department of Electronics and Communication Engineering, Manipal Institute of Technology. He has nearly 21 years of experience till date. His research interests include microstrip antennas and wireless communication systems.

SAMEENA PATHAN is currently an Assistant Professor with the Department of Information and Communication Technology, Manipal Institute of Technology, Manipal Academy of Higher Education, Manipal. Her research interests include pattern recognition, medical image analysis, artificial intelligence, and machine learning.

JAUME ANGUERA (Fellow, IEEE) was born in Vinaròs, Spain, in 1972. He received the Technical Engineering degree in electronic systems and the Engineering degree in electronic engineering from Ramon Llull University (URL), Barcelona, Spain, in 1994 and 1998, respectively, and the degree in telecommunication engineering and the Ph.D. degree in telecommunications from the Polytechnic University of Catalonia (UPC), Barcelona, in 1998 and 2003, respectively. He is a Founder and a CTO with Ignion and an Associate Professor with URL. From 1997 to 1999, he joined the Electromagnetic and Photonic Engineering Group, Signal Theory and Communications Department, UPC, as a Researcher in microstrip fractal-shaped antennas. In 1999, he was a Researcher with Sistemas Radiantes, Madrid, Spain, where he was involved in designing dual-band dual-polarized fractal-inspired microstrip patch arrays for mobile communications. In the same year, he became an Assistant Professor with the Department of Electronics and Telecommunications, URL, and an Associate Professor, in 2016, where he is currently teaching antenna theory and related courses and belongs to the recognized Research Group Smart Society. His biography is listed in Who'sWho in the World, Who'sWho in Science and Engineering, Who'sWho in Emerging Leaders, and International Biographical Center (IBC), Cambridge-England. He is the working group "Software and Modeling" Vice-Chair at EurAAP. He is a reviewer of several IEEE journals and others. He is an Associate Editor of IEEE OPEN JOURNAL ON ANTENNAS AND PROPAGATION and ELECTRONICS LETTERS. He is an IEEE Antennas and Propagation Distinguished Lecturer.

● ● ●